MAINSHOCK-AFTERSHOCK STATE-DEPENDENT FRAGILITY CURVES: A CASE OF WOOD-FRAME HOUSES IN BRITISH COLUMBIA, CANADA

Lizhong Zhang[1], Katsuichiro Goda[2,3], Flavia De Luca[1], and Raffaele De Risi[1]

[1]Department of Civil Engineering, University of Bristol, Bristol, United Kingdom
[2]Department of Earth Sciences, University of Western Ontario, London, Canada
[3]Department of Statistical & Actuarial Sciences, University of Western Ontario, London, Canada

During a mainshock-aftershock (MSAS) sequence, there is no time to retrofit structures that are damaged by a mainshock, therefore, aftershocks could cause additional damage. This study proposes a new approach to develop state-dependent fragility curves using real MSAS records. Specifically, structural responses before and after each event of MSAS sequences are used to obtain statistical relationships among the engineering demand parameter prior to the seismic event (*pre-EDP*), the intensity measure of the seismic event (*IM*), and the engineering demand parameter after the seismic event (*post-EDP*). The developed fragility curves account for damage accumulation, providing the exceeding probability of damage state (DS) given the *IM* of the event and the DS of the structure prior to the seismic excitation. The UBC-SAWS model, which was developed for wood-frame houses in British Columbia, Canada, is considered as a case study application. Results indicate that, for the examined structural typology, state-dependent fragility curves based on residual inter-storey drift ratio (*pre-EDP*), peak ground velocity (*IM*), and maximum inter-storey drift ratio (*post-EDP*) are the best choice to characterise the cumulative damage effect. An illustration of the developed fragility curves is provided by considering a hypothetical MSAS scenario of a M_w 9.0 Cascadia mainshock triggering a M_w 6.0 crustal event in the Leech River fault, affecting wooden houses in Victoria, Canada. The MSAS scenario increases Yellow tags (restricted access) by 12.3% and Red tags (no access) by 4.8%.

KEYWORDS

State-dependent aftershock fragility curves, real mainshock-aftershock sequences, nonlinear dynamic analysis of wood-frame houses, cloud analysis, multinomial distribution

1 INTRODUCTION

Recent M_w 9.0 earthquake sequences, such as the 2011 Tohoku earthquake sequence, showed the destructive effects of aftershocks on buildings [1,2]. Cumulative damage due to aftershocks can have a significant impact on the post-earthquake risk assessment immediately after a mainshock, for example, building tagging, inspection prioritisation, re-occupancy decision, and retrofitting [3–7]. Similar destructive mainshock-aftershock (MSAS) sequences could occur in other subduction zone regions. For instance, based on turbidite records in the past 10,000 years, the Cascadia subduction zone (CSZ) from Vancouver Island to Northern California ruptured 19 times with M_w 9.0-class earthquakes [8], resulting in an average recurrence period of 526 years. To account for the cumulative damage of MSAS sequences, a fragility model that can estimate the DS of a structure after each event during an earthquake sequence is necessary.

Many studies have focused on the cumulative damage effects of aftershocks on different types of structures [9–12]. Among these, Luco *et al.* (2004) developed a set of state-dependent fragility curves by using non-linear dynamic analysis. A steel moment-resisting frame model was subjected to scaled mainshock records to attain different levels of damage (referred as pre-DSs, i.e., the damage registered as a result of the mainshock). Following that, aftershock records (which were identical to the mainshock record set) were applied to the mainshock-damaged building by performing incremental dynamic analysis (IDA) attaining cumulative damage resulting from the sequence (referred as post-DSs, i.e., the damage on the structure subjected to the aftershocks). This is so-called back-to-back application of mainshock records [10]. The cumulative damage effects due to aftershocks were captured by the damage accumulation from the pre-DS (characterised by *pre-EDP*) to the post-DS (characterised by *post-EDP*). Raghunandan *et al.* (2015) extended Luco *et al.*'s approach to a reinforced concrete building by modelling it as a nonlinear multi-degree-of-freedom system and used the maximum inter-storey drift ratio (MaxISDR) as *EDP*. Ebrahimian *et al.* (2014) developed a performance-based framework for aftershock risk forecasting which consists of an epidemic-type aftershock sequence model and event-based aftershock fragility curves [7]. The ground motion records that were constructed for developing event-dependent aftershock fragility curves were selected from the pool of observed aftershock events.

The procedure by Luco *et al.* (2004) facilitates various post-earthquake decision-making, such as building-tagging and seismic loss estimation. However, there are four aspects that can be improved. (1) Since the aftershock

records from the back-to-back application are constructed from mainshock records, the link between the pre-structural response by the mainshock and the post-structural response by the aftershock is eliminated. Thus, real MSAS records are desirable. (2) The *post-EDP* may be overestimated, when the back-to-back application of mainshock records is used for aftershock records with IDA [13]. (3) The computational cost of the back-to-back approach with IDA is high [12]. (4) An appropriate set of *IMs* and *EDPs* needs to be selected to represent the intensity of ground motions and structural responses, respectively. The spectral acceleration (Sa) at the fundamental period of a structure is widely used as *IM* [14–16]. However, using a single-period Sa may not be effective, because higher mode effects and period elongation of the structure are also important [17], and a sufficient *IM* would allow to amplify records with moderate scaling factors to have more data points without causing significant biases [18]. Therefore, other *IMs*, such as Arias intensity (AI), cumulative absolute velocity (CAV), spectral intensity (SI), and peak ground velocity (PGV), should be taken into consideration in identifying the most suitable *IM* for the development of state-dependent aftershock fragility curves.

This study develops a new approach to produce the state-dependent fragility curves due to real MSAS sequences, which can be implemented to perform short-term post-earthquake risk assessments in major subduction zones. The novelties of this study are that (1) a large set of real MSAS sequences with wide ranges of rupture distances (0-270 km) and magnitudes (5.0-9.0) is used for the fragility assessment. (2) Rather than attaining each pre-DS with scaled mainshock records [10], structural responses before and after each event due to the real MSAS sequences with moderate scaling factors are used to obtain *pre-EDP – IM – post-EDP* sets for the development of state-dependent fragility curves. (3) To reduce the computational cost from the back-to-back approach, a new approach that adopts cloud analysis [19] with moderate scaling factors to scale the entire real MSAS sequences is proposed to develop the state-dependent fragility curves. The 3D dataset (*pre-EDP – IM – post-EDP*) is binned according to the same pre-DS. For each *IM – post-EDP* dataset that is classified by the same pre-DS, *IM* values corresponding to specific *post-EDP* intervals are then fitted using the lognormal distribution and multinomial distribution [20,21] to produce the state-dependent fragility curves. (4) Different combinations of *IMs* and *EDPs* are evaluated in developing state-dependent seismic fragility curves given the *pre-EDP – IM – post-EDP* sets from the real MSAS sequences.

The procedure of developing state-dependent fragility curves for MSAS sequences is applied to wooden houses in British Colombia, Canada that are represented by the UBC-SAWS (seismic analysis of wood-frame structure) models. The wood-frame house is selected, because 56% of buildings in British Columbia are wood-frame houses, 40% of which were built before 1970 [22]. Since seismic provisions of the National Building Code of Canada were adopted and enforced in British Columbia after 1973, the majority of old residential houses can be considered as 'non-engineered' from seismic design viewpoints. Consequently, many wood-frame houses with low seismic resistances may suffer significant damage due to a M_w 9.0 mainshock and aftershocks in the CSZ.

This paper is organised as follows. A general description of the new approach to develop the state-dependent fragility curves is given in Section 2. To demonstrate the new approach, the input ground motion records and UBC-SAWS model are also described in Section 2. After identifying the appropriate *EDP* and *IM* for the SAWS model in Section 3, Section 4 implements the new approach to develop the state-dependent fragility curves and presents the results of deriving such fragility curves for the wood-frame houses in British Columbia, Canada.

2 METHODOLOGY

2.1 Procedures to develop the state-dependent fragility curves

A general procedure to develop the state-dependent fragility curves is illustrated below:

- Real records of subduction-crustal MSAS sequences from local or global record datasets at the target site are gathered. Such MSAS can later be used as real or scaled records with moderate scaling factor values;
- Non-linear structural dynamic analyses of a target building model using the MSAS sequences are performed;
- Structural responses before and after each event and the intensity measure of each event during a sequence are recorded and used to develop statistical *pre-EDP – IM – post-EDP* relationships;
- The efficiency and sufficiency of the *IM* associated with the *post-EDP* are examined. This allows using moderate scaling factors for cloud analysis to reduce the high computational cost from IDA;
- Since *EDPs* can be associated with the DS of the structure, before developing the state-dependent fragility curves, the pre-DS and post-DS associated with *pre-EDP* and *post-EDP* are defined.
- Finally, the 3D dataset (*pre-EDP – IM – post-EDP*) is binned according to the same pre-DS; for each bin, *IM* values corresponding to specific post-DSs are then fitted progressively using different functional forms (e.g., lognormal and multinomial functions) to produce the fragility curves.

To illustrate the key concept of cumulative damage due to repeated earthquakes and the potential application of state-dependent fragility, a schematic diagram of cumulative damage by multiple events is shown in **Figure 1** [10,23]. The residual capacity of the structure may be decreased as more events affect the structure. For instance, for the first shock, the structure starts from an undamaged condition, and therefore, given IM_1 of the first event only, the post-DS after the first event can be estimated. More in general, with IM_j of the j-th shock and pre-DS_i before the j-th shock, the post-DS_i can be evaluated, and this procedure can be applied recursively.

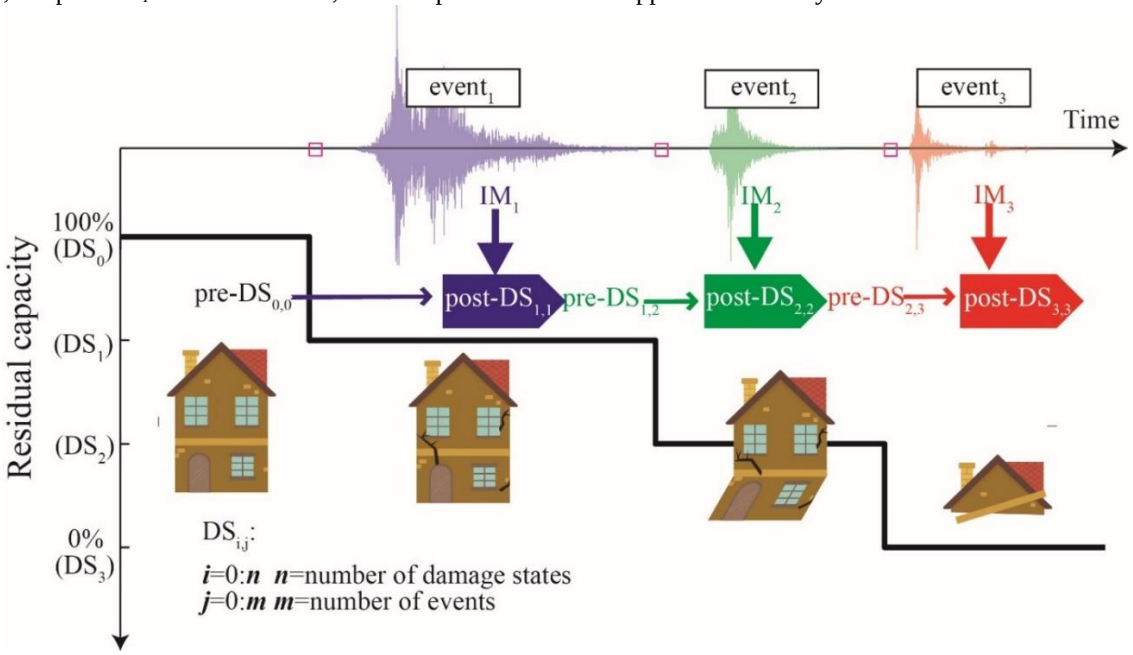

Figure 1. Illustration of damage accumulation due to a mainshock-aftershock sequence.

2.2 Mainshock-aftershock ground motion records

Using appropriate ground motion records to represent real MSAS sequences is important for seismic demand estimation. The real MSAS record datasets from [24] and [25] are described in this section, which consist of 596 MSAS sequences of real earthquakes. The magnitude-distance plots of the 596 mainshocks (with filled markers) and 1,685 aftershocks (with unfilled markers) are shown in **Figure 2** by distinguishing between the PEER-NGA database, in which only crustal records are provided, and Japanese K/KiK/SK-net database, where all crustal, in-slab and interface records are available. Crustal earthquakes from the NGA and K/KiK/SK-net databases have lower magnitudes and shorter distances than the interface and in-slab events from the K/KiK/SK-net database. The 596 records from this study have a magnitude range of 5.0-9.0 from different types of events, and include the 2011 M_w 9.0 Tohoku sequences with rupture distances up to 270 km. There are 2,281 events (202 crustal NGA events, 374 crustal-K/KiK/SK events, 1,538 interface events, and 167 in-slab events) from 596 sequences × 2 horizontal components, thus 4,562 *pre-EDP – IM – post-EDP* triplets (1,192 mainshocks and 3,370 aftershocks) can be obtained.

The design spectrum with site class C in Victoria [26] and response spectra with median and $16^{th}/84^{th}$ percentiles of mainshocks and aftershocks are shown in **Figure 3(a)**. Because some large subduction earthquake records (e.g., the 2011 Tohoku event with M_w 9.0) were recorded hundreds of kilometres away from the record stations, the response spectra of the mainshocks is not strong in comparison with the design spectrum. The response spectra of the mainshocks are generally higher than those of the aftershocks. Such inherent characteristics of natural records should be automatically incorporated in developing state-dependent seismic fragility curves using the above defined sets of MSAS series. **Figure 3**(b) shows the response spectra of median and $16^{th}/84^{th}$ percentiles of all earthquake types without distinction between mainshocks and aftershocks.

Since the median response spectra of the aftershocks are smaller than the mainshocks, scaling factors are necessary to ensure that the structure reaches collapse state for the development of fragility curves. Unlike other IDA studies [19,27] that performed detailed record selection (e.g., CMS) and allowed high scaling factors up to 10, this study uses cloud analysis [28] and applies moderate scaling factors to the entire MSAS sequences. Vamvatsikos and Cornell (2002) indicated that the sufficiency of *IM* is important to allow a high scaling factor for record scaling. In this study by selecting the sufficient and efficient *IM* and the most suitable *EDP* from Section 3, moderate scaling factors of up to 5 are considered to be acceptable for cloud analysis, as suggested by other studies [19,29].

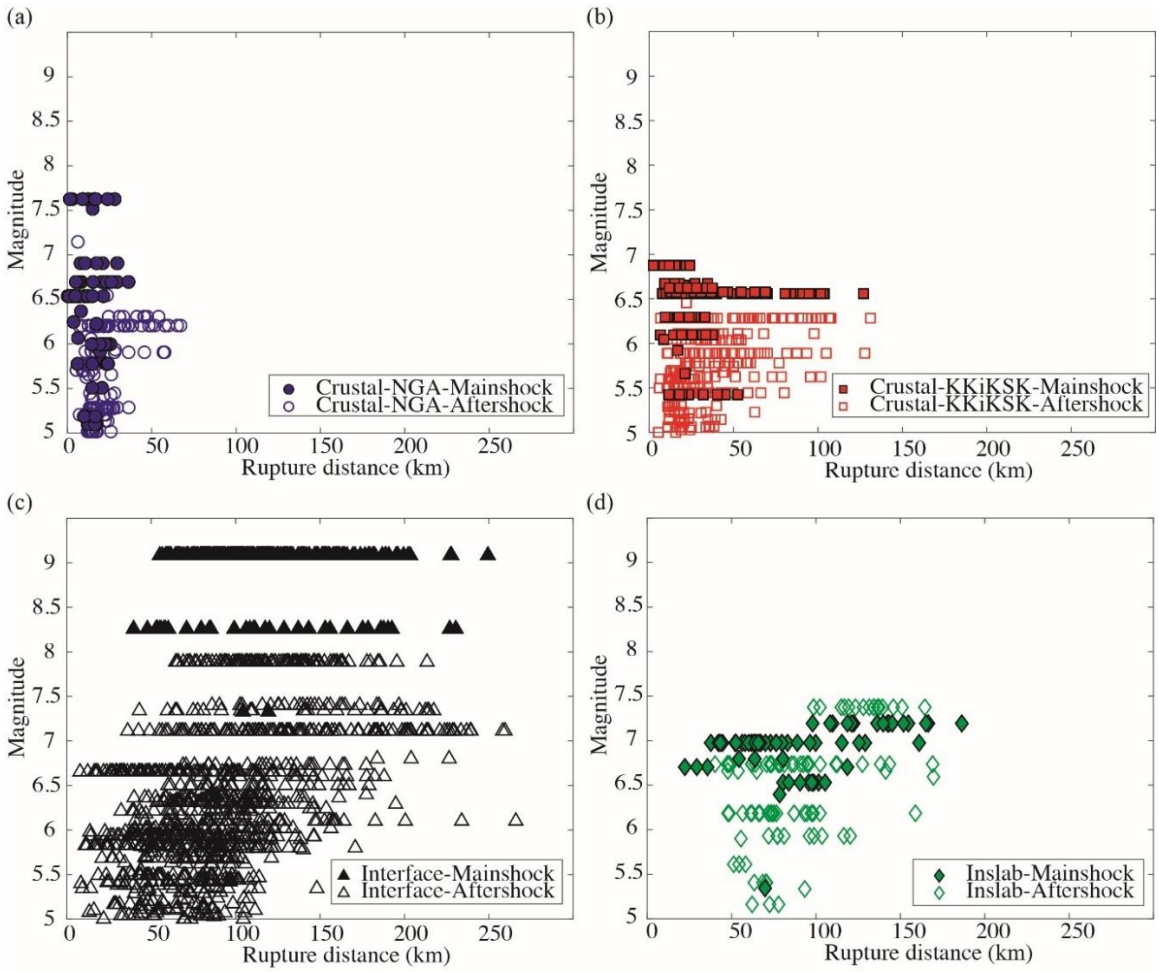

Figure 2. Magnitude-distance plot of the mainshocks (with filled markers) and aftershocks (with unfilled markers) including (a) crustal-NGA, (b) crustal-K/KiK/SK, (c) interface, and (d) inslab events.

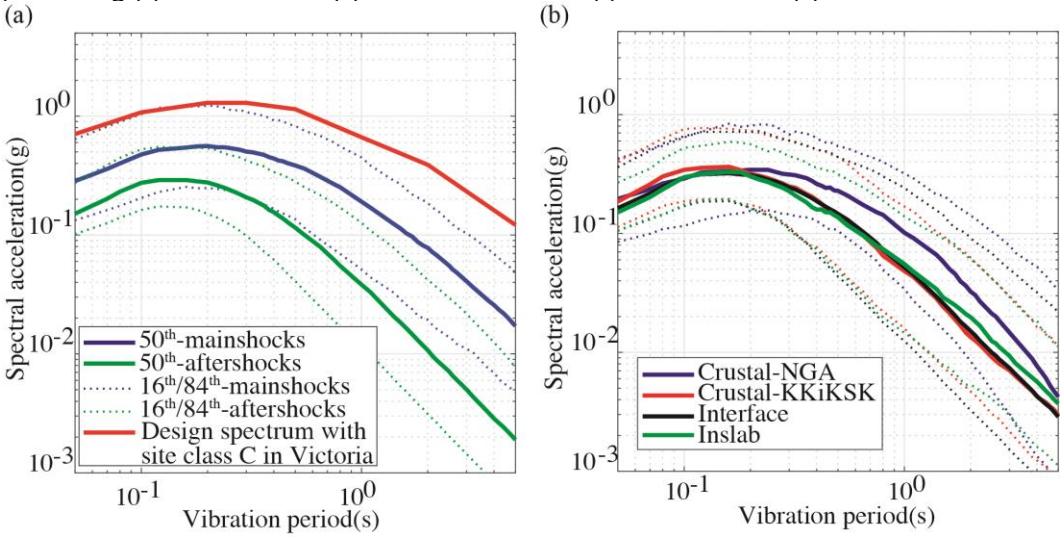

Figure 3. Response spectra (a) of mainshocks and aftershocks with 16th, 50th, and 84th percentiles, and design spectrum with site class C in Victoria (b) of different earthquake types from both mainshocks and aftershocks with 16th, 50th, and 84th percentiles.

2.3 UBC-SAWS model

The UBC-SAWS model is a structural model of typical wood-frame houses in British Columbia, Canada [30]. It is based on the SAWS model [31,32] with modifications of the model parameters for Canadian wooden house construction. The basic assumptions of the UBC-SAWS model are: (1) floor and roof diaphragms are rigid (length = 7.62 m, width = 6.10 m, and height = 2.74 m), (2) bi-directional horizontal seismic excitations are considered but ignoring vertical excitations, and (3) shear walls are represented by nonlinear springs, hysteresis of which is characterised by the Cyclic Analysis SHEar Walls (CASHEW) model [33] (see **Figure 4**). The CASHEW model incorporates stiffness and strength degradation. However, no in-cycle degradation is considered in the hysteresis model. The parameters of the UBC-SAWS model were calibrated based on static and dynamic tests of wall panels with different configurations and shake-table tests of full-scale houses that were conducted at the University of British Columbia [30]. The sheathing materials of the shear wall include horizontal board (shiplap), gypsum wallboard (GWB), plywood, oriented strand board (OSB), and stucco.

Based on different shear-wall configurations, four types of two-storey wood-frame houses are defined in the UBC-SAWS model: (1) House 1 with stucco/engineered OSB/GWB, (2) House 2 with engineered OSB/GWB, (3) House 3 with non-engineered OSB/GWB, and (4) House 4 with horizontal boards/GWB. The term 'engineered' for Houses 1 and 2 indicates that hold-downs and blocking of the wall panel are used to increase its seismic resistance and to meet the seismic code requirements. Due to the design layout of the house model in **Figure 4**(b) (e.g., dimensions of the house along x-axis and y-axis and locations of windows and doors), the stiffness along x-axis is smaller than that along y-axis, and the expected failure mode of the house models is the soft-storey collapse of the ground floor level due to larger openings. The fundamental vibration periods along x-axis of Houses 1-4 are 0.25 s, 0.3 s, 0.35 s, and 0.4 s, respectively, whereas those along y-axis are about 0.22 s for all houses [30]. In **Figure 4**(b), 16 walls (W1-W16), which are represented by nonlinear springs, are present along x-axis and y-axis on the ground and first floors. Shear-walls along x-axis are different for Houses 1-4 (W1 to W7), whereas shear-wall elements along y-axis are the same for the four house models (W8 to W16) [27]. The pushover analysis results of Houses 1-4 by using the inverse triangle load distribution are shown in **Figure 4**(c). The base shear ratio in vertical axis is the ratio of the base shear force and the total weight of the house. In terms of pushover curves, House 1 has the highest seismic capacity; Houses 2 and 3 have similar seismic resistance; and House 4 has the lowest seismic capacity. A recent study by [34] indicated that House 4 with horizontal boards is not suitable in high seismic regions and median collapse capacities of House 4 is reduced by 61% under long-duration motions in comparison with short-duration motions.

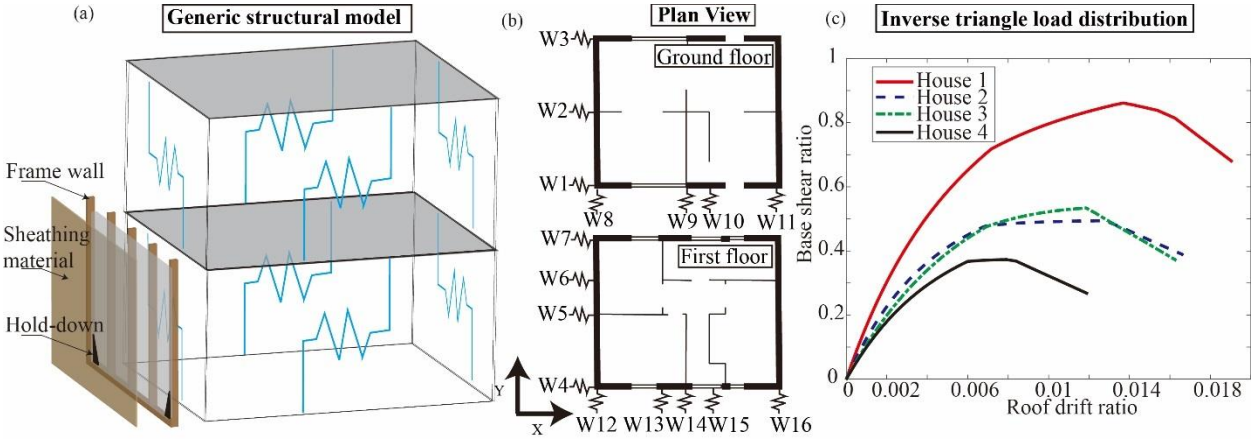

Figure 4. Illustration of the UBC-SAWS model: (a) generic model of wood-frame houses, (b) ground and first floor plans of wood-frame houses, and (c) pushover analysis of Houses 1-4.

2.4 Evaluation of *IM*s

To evaluate different *IM*s, various studies have focused on the efficiency, sufficiency, and relative sufficiency of *IM* [15,16,35]. Efficiency means that the prediction variability of *EDP* is small given *IM*, which can potentially reduce the number of structural response analyses. Consider a linear relationship between *IM* and *EDP* in logarithmic scale (base 10):

$$\log_{10}(EDP) = \log_{10}(a_{IM}) + b_{IM} \times \log_{10}(IM) \quad (1)$$

where a_{IM} and b_{IM} are the coefficients of the linear regression. The efficiency is calculated by [35]:

$$\beta_{IM} = \sqrt{\frac{\sum_{i=1}^{m}(\log_{10}(EDP_i) - \log_{10}(a_{IM} \times IM_i^{b_{IM}}))^2}{m-2}} \quad (2)$$

Sufficiency of *IM* indicates that the *EDP* is independent of other explanatory variables, such as rupture distance and magnitude, when *IM* is taken into account. Therefore, if *IM* is sufficient, the inclusion of other variables, in addition to the main *IM*, does not affect the distribution of *EDP*. To evaluate the sufficiency of *IM*, the residual (Res_{IM}) between *IM* and *EDP* from **Equation (1)** is calculated as:

$$Res_{IM} = \log_{10}(EDP) - \log_{10}(a_{IM} \times IM^{b_{IM}}) \quad (3)$$

Following that, the dependency of Res_{IM} on rupture distance (R_{rup}) and magnitude (M_w) can be examined by:

$$Res_{IM} = c_{IM} + d_{IM} \times \log_{10}(R_{rup}) \quad (4)$$

$$Res_{IM} = c_{IM} + d_{IM} \times M_w \quad (5)$$

where c_{IM} and d_{IM} are the coefficients of the regression. The sufficiency of *IM* can be quantified by the significance level (p_{IM}-value) for d_{IM} [16].

Moreover, Jalayer *et al.* (2012) proposed relative sufficiency as a measure to compare the sufficiency between different IMs based on the concept of relative entropy from information theory. The relative sufficiency between two *IM*s is calculated by:

$$I(IM_j|IM_k) = \frac{1}{m} \times \sum_{i=1}^{m} log_2 \left(\frac{\beta_{IM_k} \times \phi\left(\frac{\log_{10}(EDP_i) - \log_{10}(a_{IM_{j.i}} \times IM_{j.i}^{b_{IM_{j.i}}})}{\beta_{IM_j}} \right)}{\beta_{IM_j} \times \phi\left(\frac{\log_{10}(EDP_i) - \log_{10}(a_{IM_{k.i}} \times IM_{k.i}^{b_{IM_{j.i}}})}{\beta_{IM_k}} \right)} \right) \quad (6)$$

where IM_j and IM_k represent different *IM*s, and β_{IM} is calculated from **Equation (2)**.

2.5 Seismic fragility functions

Using the selected ground motion records (Section 2.2) and the structural models (Section 2.3), 23,840 nonlinear dynamic analyses (= 4 house models × 596 MSAS sequences × 2 horizontal components × 5 scaling factors) are performed. The calculated structural responses are obtained for developing state-dependent seismic fragility functions as described in Section 2.1. The *pre-EDP*, *IM*, and *post-EDP* are selected and evaluated based on the different types of structural models and the preference of the modeller. The choice of the *IMs* and *EDPs* of SAWS model are further investigated in Section 3. To develop the post-DS fragility models in terms of associated *IM* and pre-DS, two methods are used as in Sections 2.5.1 and 2.5.2.

2.5.1 Lognormal distribution

The lognormal distribution has been widely used to fit seismic fragility curves [20]. The advantages of using the lognormal distribution for the fragility curve fitting are that (1) it is easy to apply because it has a simple format with a median and a logarithmic standard deviation as model parameters, and (2) it usually fits the data reasonable well [36]. The lognormal distribution is defined as:

$$P(DS_i) = \Phi\left(\frac{\ln\left(IM/\theta_{IM}\right)}{\beta_{IM}} \right) \quad (7)$$

where Φ is the standard normal distribution, and θ_{IM} and β_{IM} are the median value and the standard deviation of the post-DS_i fragility curves, respectively.

2.5.2 Multinomial distribution

The multinomial distribution has been applied in recent studies on fragility modelling [21,37]. In comparison with the lognormal distribution, the advantages of the multinomial distribution are that (1) it does not require binning of *IM*, so the pair of IM_i and post-DS_i given the same pre-DS can be used directly to estimate the coefficients of the

multinomial distribution, and (2) since it can accommodate the hierarchical nature of damage state severity, derived fragility curves do not intersect. The multinomial probability distribution is given by:

$$P(DS_i) = \frac{1}{\prod_{j=1}^{nDS} y_{ij!}} \cdot \prod_{j=1}^{nDS} \pi_{ij}^{y_{ij}} \quad (8)$$

where *nDS* is the total number of DS, y_{ij} is the number of data points in the *i*th *IM* falling in DS_j, and π_{ij} is the probability that the *i*th observation is in DS_j. The systematic component of the model is represented by a link function:

$$f(\pi_{ij}) = \theta_{j,0} + \sum_{k=i}^{nP} \theta_{j,k} \cdot \chi_k \quad (9)$$

where θ is the regression parameter, *nP* is the number of explanatory variables χ. The explanatory variable can be *IM*, structure type, and pre-DS if a large number of data points are available. Taking the mainshock fragility curves with $DS_{0:n}$ as an example, $\theta_{j,0}$ is the intercept terms for the relative probability of DS_i given the reference $DS_{i+1:n}$. $\theta_{j,k}$ is the coefficient of the explanatory variable, which is the mainshock *IM* in this example, and shows the probability of DS_i versus $DS_{i+1:n}$ in the log scale as the *IM* increases.

3 EVALUATION OF *EDP – IM* TRIPLETS USING REAL GROUND MOTION RECORDS

This section presents the preliminary exploratory phases of the model development by introducing *pre-EDP*, investigating the suitability of *EDPs* for *pre-EDP* and *post-EDP*, and evaluating the efficiency and sufficiency of *IMs*.

3.1 Pre-EDP

The conventional seismic fragility assessment for mainshock ground motions requires *IM* and *post-EDP* (e.g., only $event_1$ in **Figure 5**(a)). To derive state-dependent aftershock fragility curves, a suitable *pre-EDP* needs to be specified. **Figure 5**(a) illustrates a MSAS sequence from the Tohoku sequence, and **Figure 5**(b) and (c) display the structural displacement response time-history and hysteretic response, respectively, using the UBC-SAWS model for W1 on the ground floor of House 4.

Since the failure mode of the SAWS model is the soft-storey collapse of the ground floor level, three *EDPs* suitable to describe such a mechanism are selected: (a) the maximum inter-storey drift (MaxISDR) at the first level, (b) the residual inter-storey drift (ResISDR) at the first level, and (c) the maximum difference between MaxISDR and ResISDR (MaxIISDR) at the first level. **Figure 5**(b) shows the maximum, residual, and maximum incremental displacements of W1 for an illustrative earthquake sequence consisting of 3 events. $MaxISDR_1$ and $MaxIISDR_1$ of the first event are identical, because the residual displacement before the first event is zero. If the residual displacement is small, MaxIISDR becomes similar to MaxISDR.

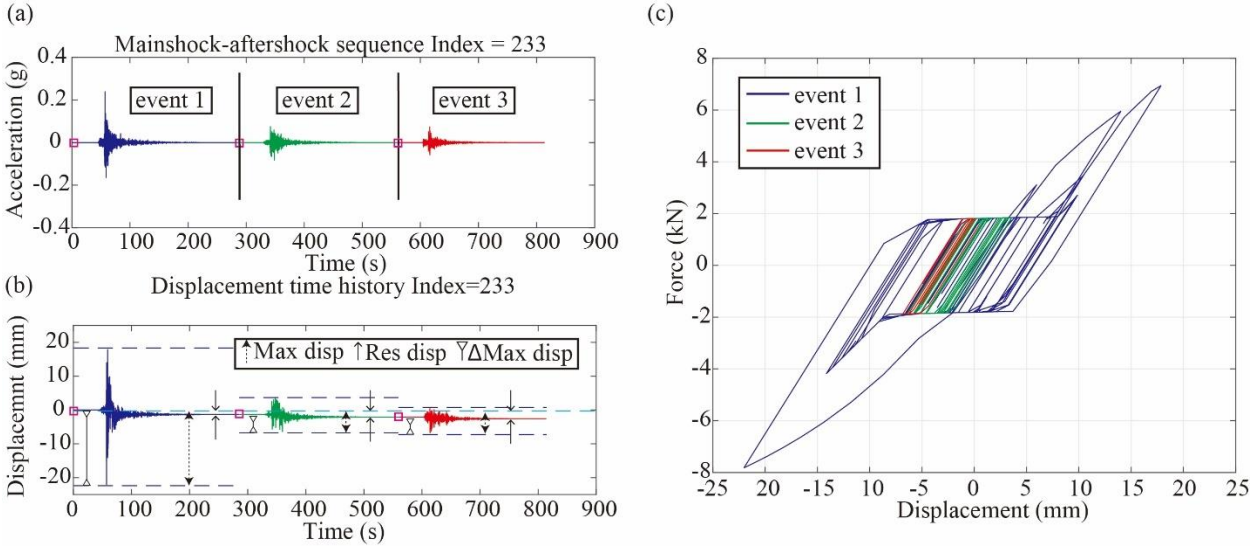

Figure 5. (a) An example of the 2011 Tohoku mainshock-aftershock sequence with (b) the displacement response time-history of House 4 of the maximum displacement (Max disp), the residual displacement (Res disp) and the incremental maximum displacement (Δ Max disp), and (c) hysteretic response plot of Events 1-3.

3.2 Evaluation of EDPs

Different combinations of *EDPs* for pre- and post-earthquake conditions are assessed by focusing upon three *EDPs*, i.e., MaxISDR, ResISDR, and MaxIISDR. In total, 9 combinations of *pre-EDP* and *post-EDP* are considered: Case 1-MaxISDR and post-MaxISDR, Case 2-pre-MaxIISDR and post-MaxISDR, Case 3-pre-ResISDR and post-MaxISDR, Case 4-pre-MaxISDR and post-MaxIISDR, Case 5-pre-MaxIISDR and post-MaxIISDR, Case 6-pre-ResISDR and post-MaxIISDR, Case 7-pre-MaxISDR and post-ResISDR, Case 8-pre-MaxIISDR and post-ResISDR, and Case 9-pre-ResISDR and post-ResISDR. These are displayed as a scatter plot where each *pre-EDP – post-EDP* point is associated with Sa(T=0.3 s) as *IM* (i.e. the coloured grading in **Figure 6**). According to **Figure 6**(a) and (b), the plots of *pre-EDP – IM – post-EDP* datasets from Cases 1 and 2 are similar. This is because (1) $MaxISDR_1$ and $MaxIISDR_1$ of the first event are identical given the residual displacement before the first event is zero, and (2) if the residual displacement is small, the MaxISDR and MaxIISDR tend to be similar. The same observation can be seen from Cases 4 and 5, and Cases 7 and 8.

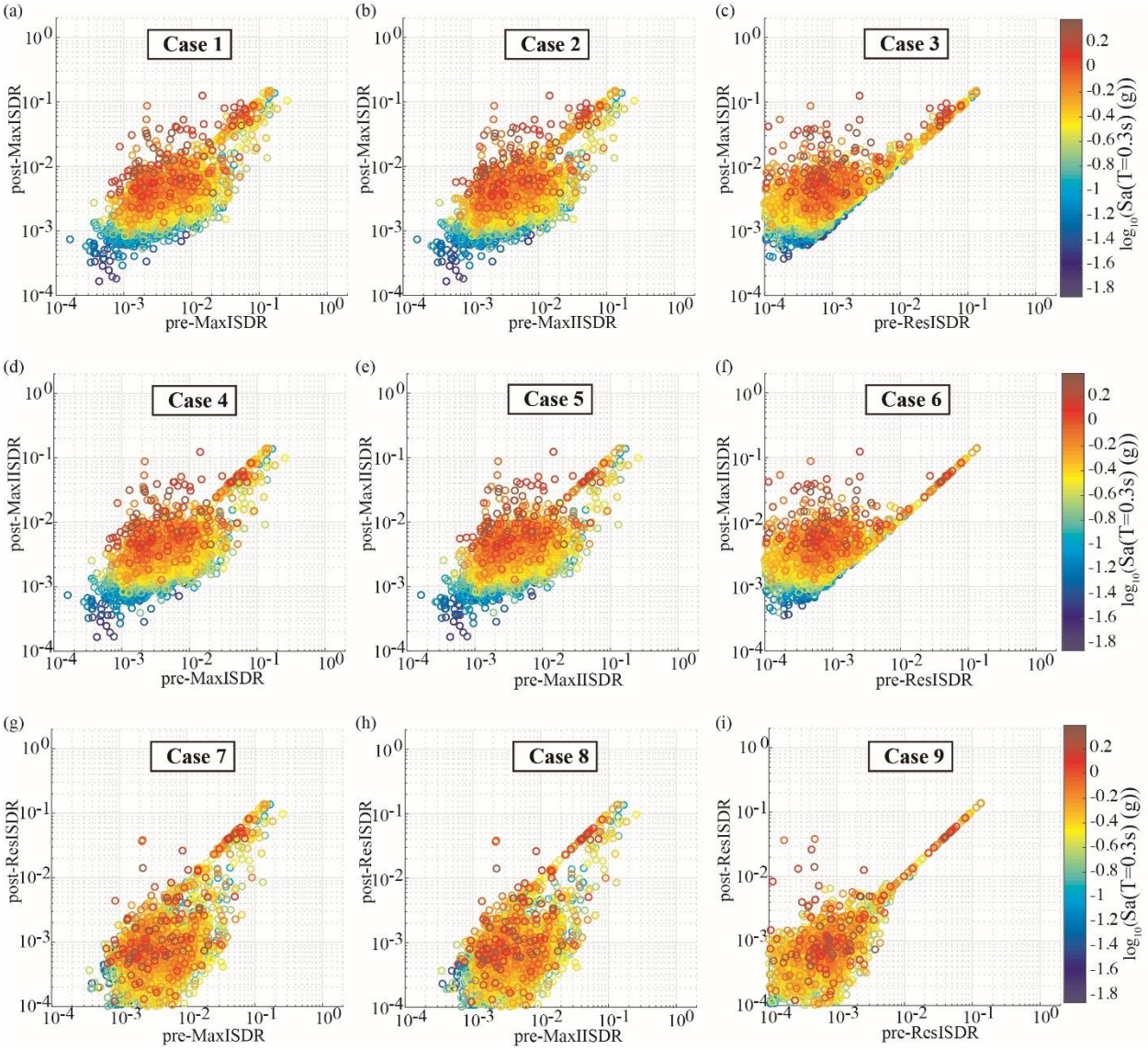

Figure 6. Plots of 9 cases of post-*EDP*s against pre-*EDP*s for House 4. (a) pre-MaxISDR and post-MaxISDR, (b) pre-MaxIISDR and post-MaxISDR, (c) pre-ResISDR and post-MaxISDR, (d) pre-MaxISDR and post-MaxIISDR, (e) pre-MaxIISDR and post- MaxIISDR, (f) pre-ResISDR and post-MaxIISDR, (g) pre-MaxISDR and post-ResISDR, (h) pre-MaxIISDR and post-ResISDR, and (i) pre-ResISDR and post-ResISDR.

Individual *pre-EDP*$_i$ should represent the DS of the structure from event$_1$ to event$_i$. In other words, since *IM* is the only input of the current fragility simulation framework, *pre-EDP* that only represents the DS of individual event$_i$ is not suitable for the state-dependent aftershock fragility curves. In this regard, MaxIISDR$_i$ that only describes the relative DS between event$_{i-1}$ and event$_i$ may not be appropriate as *pre-EDP*. Based on that, Cases 2, 5, and 8 are excluded from fragility fitting.

An ideal pair of *pre-EDP* and *post-EDP* should retain as many *IM–EDP* points as possible in fitting the fragility curves robustly, and a higher *pre-EDP* should correspond to a higher *post-EDP* to represent the cumulative damage due to an earthquake sequence. To include more *IM–EDP* points for the development of the fragility curves, the *EDP* pairs of Cases 3, and 6 are more suitable than Cases 1, 4, 7, and 9. This is because the points in Cases 1, 4, 7, and 9 need to be divided into two parts which are *pre-EDP* > *post-EDP* and *pre-EDP* < *post-EDP*, respectively. The former would be no damage scenario and only the latter part can be used for the aftershock fragility development. On the other hand, when Cases 3 and 6 are considered in **Figure 6**(c) and (f), since the absolute maximum displacement is always larger than the absolute residual displacement, all points can be used for the development of the fragility curves, resulting in more robust curve fitting (i.e., all points are above the bisector of the quadrant).

Based on these considerations, Cases 3 and 6 are suitable options for the development of aftershock fragility curves. However, an issue of adopting Case 6 is that the post-DS definitions of MaxIISDR may need to be changed with pre-ResISDR. In other words, the DS associated with MaxIISDR is not constant given different pre-DSs, because MaxIISDR$_i$ only represents the response of event$_i$. Considering MaxIISDR has not been widely used for aftershock risk assessment in comparison with MaxISDR, in the subsequent part of this study only Case 3 (pre-ResISDR and post-MaxISDR) is considered to represent *pre-EDP* and *post-EDP*.

3.3 Evaluation of *IM*s

To evaluate different *IMs*, metrics for efficiency, sufficiency, and relative sufficiency are calculated for Sa(T=0.05-5 s), AI, CAV, PGV, and SI [16,35,38]. The non-collapse *EDP* values [39] of House 4 are used for the evaluation of *IMs* from the unscaled records of MSAS sequences, because the majority of the wood-frame houses in British Columbia are classified as House 4 with non-seismic resistance [22,30].

The efficiency is examined based on [35]. A small standard deviation (β_{IM}) in **Equation (7)** indicates less variability of the *IM–EDP* relationship (i.e., higher predictability). The values of β_{IM} in a range of 0.2 to 0.3 and 0.3 to 0.4 are considered as a good and acceptable *IM* in terms of efficiency, respectively [40]. According to **Figure 7**(a), Sa(T=0.3-0.5 s), PGV, and SI are more efficient than others for House 4.

Next, the sufficiency (p_{IM}) of *IMs* is checked against source parameters (rupture distance and magnitude) for House 4. p_{IM} captures the statistical independence between the source parameters and *IM* given p_{IM}>0.05. The sufficiency of *IMs* in terms of rupture distance and magnitude is shown in **Figure 7**(b) and (c), respectively. Sa with periods 0.2 to 2 s, PGV, and SI are good candidates of *IM*. On the other hand, Sa with periods 0.05-0.2 s and 2-5 s, AI, and CAV show a high dependence on the source parameters, which indicates that these *IMs* are not appropriate for use as sole *IM* for the fragility curve fitting of the wood-frame houses.

The relative sufficiency (I) is plotted in **Figure 7**(d) to rank different *IMs* for House 4. The fundamental period of the wood-frame house (T=0.3 s) is considered as a reference *IM*, therefore, the relative sufficiency of Sa(T=0.3 s) is 0. Sa values with periods T=0.32-1 s, PGV and SI have superior performance than Sa(T=0.3 s). Especially, Sa(T=0.4-0.5 s) and PGV have the highest relative entropy. This suggests the period elongation of the damaged structure in comparison with the fundamental period of 0.3 s. Since the most suitable *IMs* are in the range of 0.3-0.5 s and PGV shows a good performance of House 4, in this study Sa (T=0.3 s and 0.5 s) and PGV are used to derive the state-dependent fragility curves in Section 4. In addition, the selection of *IM* should also be related to the availability of the ground motion prediction equation (GMPE), when the developed fragility models are implemented for seismic risk assessments. Although PGV is not widely used for the subduction GMPEs based on the global dataset [41], other GMPEs for the CSZ have considered PGV as the output [42]. SI is also an appropriate *IM* based on the results of sufficiency and efficiency. However, SI is calculated by taking the integral of spectral accelerations over a period range from 0.1 to 2.5 s, which requires a high computational cost with the spatial correlation. In addition, the correlations between periods are also necessary, therefore, in this study SI is not considered in the development of aftershock fragility curves.

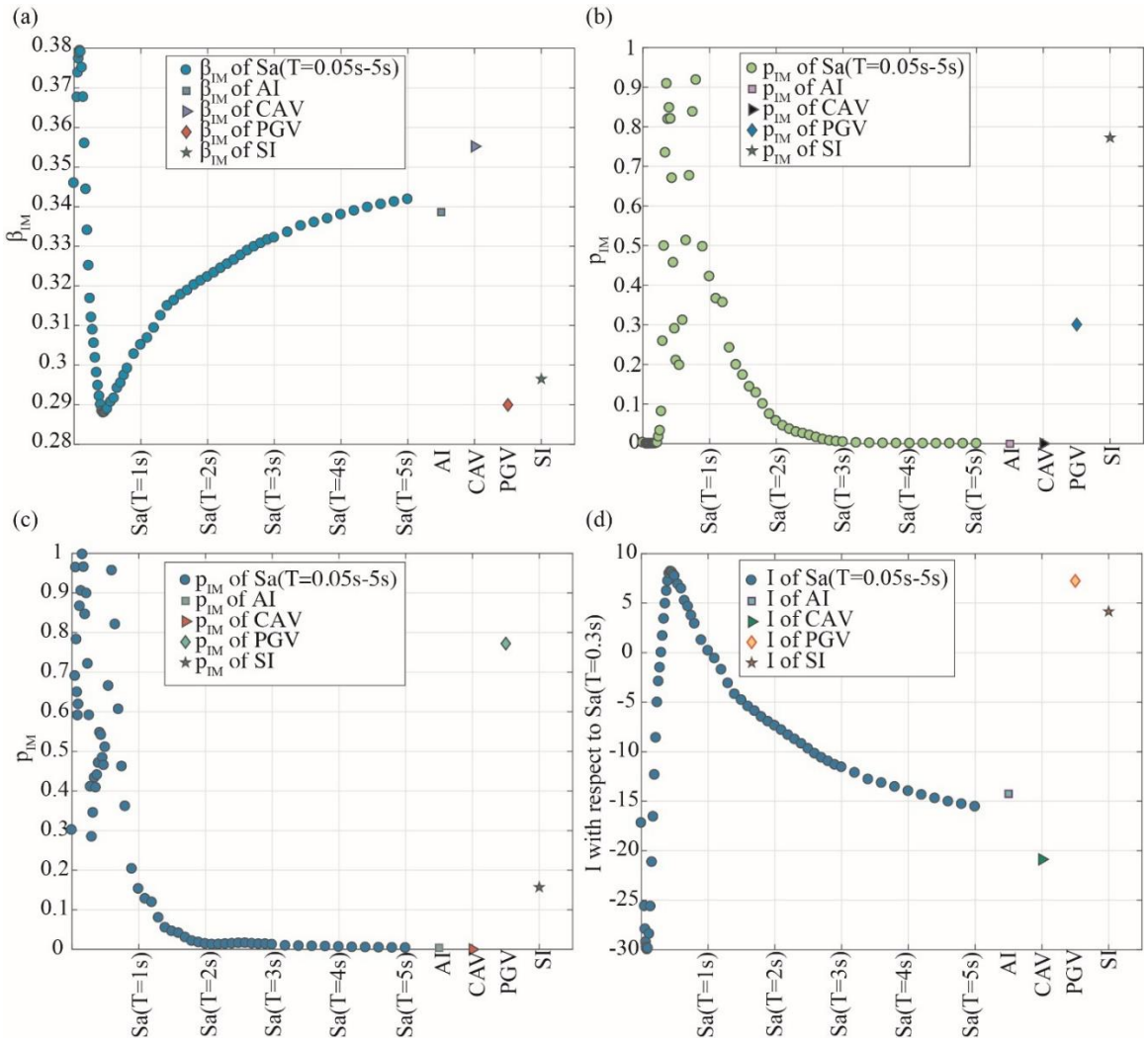

Figure 7. Plot of (a) efficiency (β_{IM}), sufficiency (p_{IM}) for (b) rupture distance and (c) magnitude, and (d) relative sufficiency (I) of each IM (Sa(T=0.05-5 s), AI, CAV, PGV, and SI) given the non-collapse EDP with unscaled records for House 4.

4 STATE-DEPENDENT FRAGILITY MODELLING

4.1 Definitions of pre-DS and post-DS

This subsection defines DSs in terms of pre-ResISDR and post-MaxISDR of Houses 1-4. Various studies investigated the relationship between ResISDR and MaxISDR for different types of structures, e.g., moment resisting steel frames and non-ductile reinforced concrete buildings [43,44]. For wood-frame houses, a FEMA study [45] defined performance level (PL) of wood stud walls based on MaxISDR. MaxISDR thresholds with PL_1-1%, PL_3-2%, and PL_5-3% are considered as immediate occupancy, life safety, and collapse prevention, respectively. In [46], the DSs of the wood-frame house associated with MaxISDR thresholds 1%, 2%, 4.5%, and 7% were defined as minor damage, significant damage, major damage, and collapse risk, respectively. In terms of the collapse state associated with MaxISDR, the collapse state of the SAWS model was defined as MaxISDR>7% in [39]. Considering different shear wall types of wood-frame houses and record durations, in [34] the collapse state of the wood-frame houses was defined based on the short and long durations of the records (same hysteretic model as this study but with modified hysteretic parameters). Regarding the DSs associated with ResISDR, $PL_{1,3,5}$ of wood stud walls were considered with the ResISDR thresholds with 0.25%, 1%, and 3% [45], while ResISDR of 0.2%, 0.5%, 1%, and 2% were suggested for $DS_{1\text{-}4FEMA}$ in [47]. In terms of building tagging for the post-earthquake evaluation, three tagging levels are usually considered, which are Green tag (unrestricted access), Yellow tag (restricted access), and Red tag (no access) [4].

Given the pushover analysis results of Houses 1-4 are significantly different in **Figure 4**(c), the DS thresholds of each house model should be defined individually based on the literature and the *IM–EDP* results from this study. The following procedures are carried out to define the DSs with MaxISDR and ResISDR of Houses 1-4 by first determining the collapse states of ResISDR and MaxISDR:

- The collapse state associated with MaxISDR for Houses 1-4 is defined by taking the average collapse state limits of short and long record durations from [34], which is 7%, 6%, 6%, and 5.5% for Houses 1-4 (**Table 1**). This is because the ground motion records used in that study include both short- and long-duration records and the application of the fragility curves would focus on both crustal and subduction-zone earthquakes.
- The collapse state associated with ResISDR for Houses 1-4 is determined by the *IM–EDP* results from this study. The 3D dataset including pre-ResISDR, Sa(T=0.3 s), and post-MaxISDR is binned according to pre-ResISDR expressed in terms of percentage (i.e., [0; 0.3], [0.3; 0.5], [0.5; 1], [1; 2], [2; 3], [3; 4], [4; 5], [5; 6], [6; 7], and [7; 8]). The linear regression of log(non-collapsed post-MaxISDR) and $a_{dsRes}+b_{dsRes}$log(Sa(T=0.3 s)) given each binned pre-ResISDR is obtained, where a_{dsRes} and b_{dsRes} are the regression coefficients. The slope (b_{dsRes}) of linear regression is used to detect the change of pre-ResISDR. Since the higher Sa(T=0.3 s) results in higher MaxISDR and ResISDR, the collapse state associated with ResISDR is determined when the slope (b_{dsRes}) of MaxISDR against Sa(T=0.3 s) given the binned pre-ResISDR is less than 0.1, which leads to 4%, 4%, 3%, and 3% for Houses 1-4.

Table 1. Collapse state limits of Houses 1-4.

	House 1	House 2	House 3	House 4
ResISDR	4%	4%	3%	3%
MaxISDR	7%	6%	6%	5.5%

By having the collapse state limits of ResISDR and MaxISDR, the ratios between three tagging levels and collapse state are provided in **Table 2** based on the DS descriptions [4,45–47]. Green tag (DS_1) can be regarded to be equivalent as immediate occupancy [4]. Yellow tag (DS_2) is the intermediate DS between life safety and collapse prevention, because Yellow tag is defined for only acceptable entry for workers doing maintenance which is beyond the life safety [3]. Red tag (DS_3) is the intermediate DS between collapse prevention and collapse because Red tag forbids assess to a damaged building and the building is assumed to be near collapse. The description of each DS is also summarised in **Table 2** based on [45], the Static and Dynamic Testing of Shear Wall Panels Project for the UBC-SAWS model [48], and the Earthquake 99 Wood-frame House Project EQ 99 Project [30]. Wall components that are described in **Table 2**, including wall frame, sheathing material, and hold-down, are shown in **Figure 4**(a).

Table 2. Summary of damage states associated with the lower limits of ResISDR and MaxISDR (CS=collapse state).

	No damage (DS_0)	Green tag (DS_1)	Yellow tag (DS_2)	Red tag (DS_3)	
ResISDR	0.01%	0.10×CS	0.30×CS	0.70×CS	
MaxISDR	0.01%	0.10×CS	0.30×CS	0.70×CS	
Performance level	No damage	Immediate occupancy	Life safety	Collapse prevention	Collapse
Description of damage state	No damage is observed.	Minor cracks are observed in sheathing materials. Hairline cracks are observed in external walls.	Studs are attached to the sheathing at end but are easy to bend in the middle. Nails partially loose and are attached to the stud for OSB of Houses 1-3. Sheathing is detached in the middle. Glass is partially damaged.	Studs are not attached to sheathing for some shear walls. Nails are pulled out on the sheathing. Some sheathing failure. Some fasteners on GWB are pushed. Glass is significantly damaged. Hold downs are loose for Houses 1-2.	Ground floor of the house is collapsed.

A scatter plot of the evaluated *EDPs* (post-MaxISDR versus pre-ResISDR) with the unscaled records for House 4, which is colour-coded based on Sa(T=0.3 s), is shown in **Figure 8**. Although all 596 MSAS sequences are

included in the structural analysis, small sample sizes with the number of points less than 100 are observed with pre-$DS_{1\text{-}2}$. This indicates that the scaling of records is necessary.

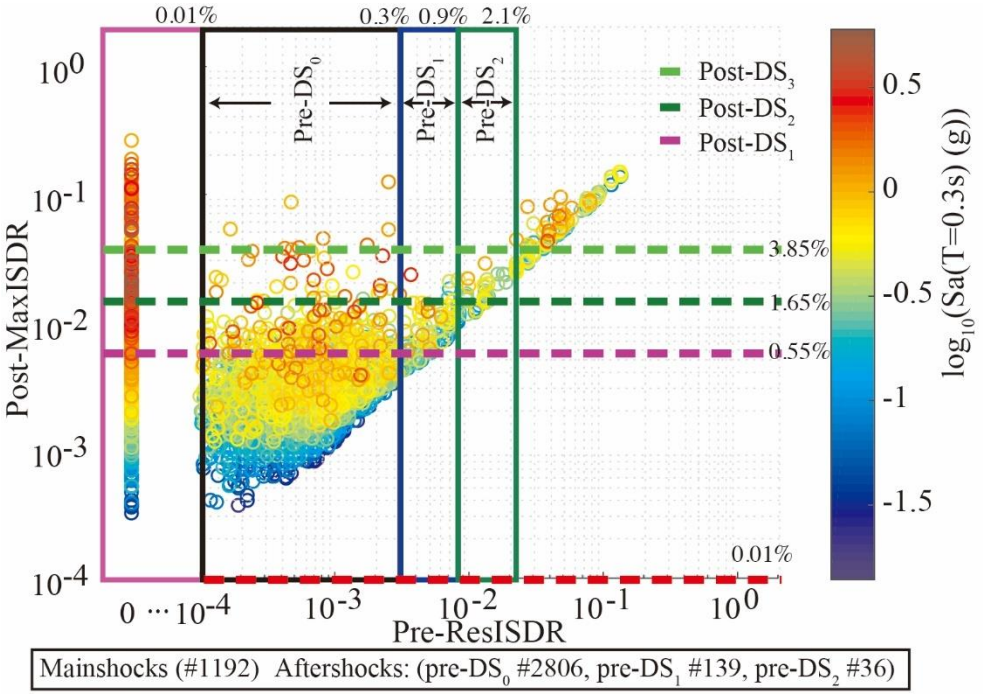

Figure 8. Plot of post-MaxISDR against pre-ResISDR with Sa(T=0.3 s) for House 4 using unscaled records. The number of points from mainshock is 1,192, and the number of points from aftershocks given pre-DS_0, pre-DS_1, and pre-DS_2 is 2,806, 139, and 36, respectively.

4.2 Procedures to develop aftershock fragility curves of wood-frame houses

Due to the insufficient data points of pre-$DS_{1\text{-}2}$ in **Figure 8**, the *pre-EDP*, *IM*, and *post-EDP* of each event during the mainshock-aftershock sequence with the scaling factors 1 to 5 are used; this leads to 4,562×5=22,810 points in total, including 5,960 and 16,850 data points for mainshocks and aftershocks, respectively. Since the frequency content of mainshocks is significantly different from that of the aftershocks (**Figure 3**), the mainshock fragility curves and the state-dependent aftershock fragility curves are produced separately. A plot of post-MaxISDR against Sa(T=0.3 s) for mainshocks only with the scaling factors 1 to 5 given pre-ResISDR=0% with post-$DS_{1\text{-}3}$ is shown in **Figure 9**(a).

The new approach to develop the state-dependent fragility curves of aftershocks is as follows:

1. The 16,850 data points in **Figure 9**(b) are classified into pre-$DS_{0\text{-}2}$ based on the pre-ResISDR bins defined in **Table 2**. The subplots of MaxISDR against Sa(T=0.3 s) for pre-$DS_{0\text{-}2}$ are shown in **Figure 10**(a)-(c).
2. For each pre-DS_i (i=0, 1, and 2), the number of post-MaxISDR > post-DS_i (i=1, 2, and 3) (i.e., exceeding the damage threshold in terms of MaxISDR in **Table 2**) is counted.
3. Two fragility functions are used to develop the fragility curves:
    a. For the lognormal distribution, fixed *IM* bins are defined for all pre-DSs in **Figure 10** to fit consistently for all pre-DS_i given the same post-DS_i. The fraction of *post-EDP* > post-DS_i (i=1, 2, and 3) from the lognormal distribution (e.g., [20]) is used to develop the fragility curves associated with *IM* for each pre-DS using the maximum likelihood estimation (MLE).
    b. The multinomial fitting based on the MLE is used to develop the post-DS curves with *IM* given the same pre-DS [21,37,49].

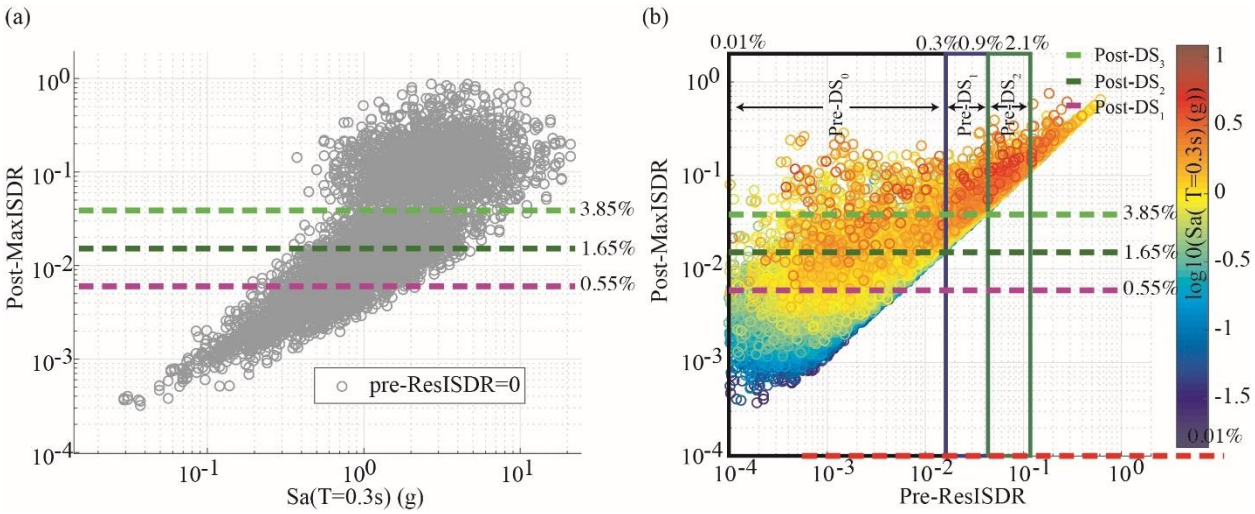

Figure 9. (a) Plot of post-MaxISDR against Sa(T=0.3 s) of House 4 for mainshocks only (596 records × 2 horizontal components × 5 scaling factors=5,960 points). (b) Plot of post-MaxISDR against pre-ResISDR for aftershocks (1,685 records × 2 horizontal components × 5 scaling factors=16,850 points).

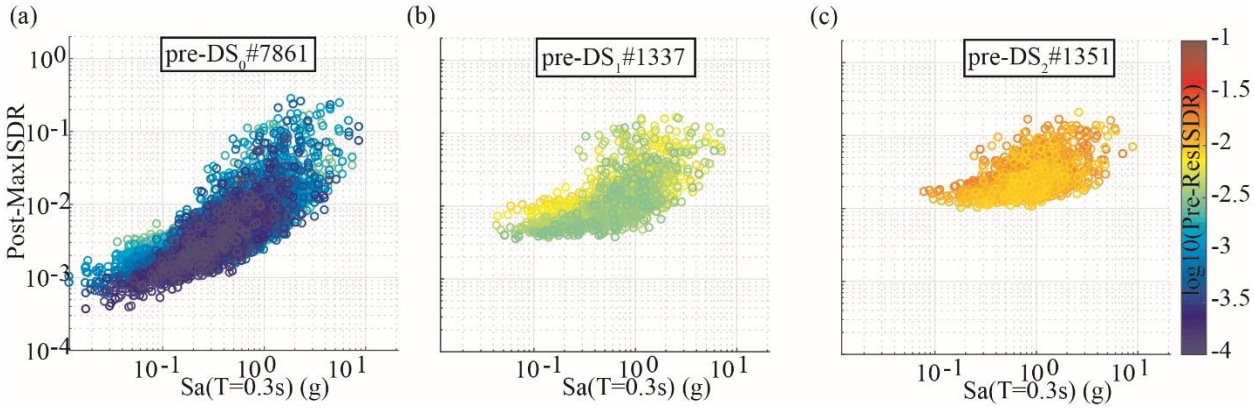

Figure 10. Plot of post-MaxISDRs against IM(T=0.3 s) for House 4 with scaling factors 1 to 5 given pre-ResISDR (a) 0.01%-0.3% (7,861 points), (b) 0.3%-0.9% (1,337 points), and (c) 0.9%-2.1% (1,351 points).

4.3 Comparison of aftershock fragility curves with Sa(T=0.3 s), Sa(T=0.5 s), and PGV

Since the state-dependent fragility curves are developed based on post-DSs given the same pre-DS, post-DSs from the same pre-DS should not intersect. Therefore, only the same post-DS_i given pre-DS_0 to pre-DS_{i-1} are presented in the following fragility curve plots. To make a fair comparison, the state-dependent fragility curves of post-DS_3 given pre-DS_0 to pre-DS_2 of House 4 with Sa(T=0.3 s), Sa(T=0.5 s), and PGV using the lognormal distribution are shown in **Figure 11**. The estimated median values (θ_{IM}) and standard deviations (β_{IM}) for post-$DS_{1\text{-}3}$ given pre-$DS_{0\text{-}2}$ with Sa(T=0.3 s), Sa(T=0.5 s), and PGV are summarised in **Table 3**. The state-dependent fragility curves with different fragility functions are presented in the next subsection (Section 4.4). The limit of x-axis is constrained by the maximum *IM* from the observed records.

The median values of Sa(T=0.3 s), Sa(T=0.5 s), and PGV decrease from pre-DS_0 to pre-DS_2 in **Table 3**, showing that the damaged house requires a low *IM* to reach the same post-DS. Although Sa(T=0.3 s) has been widely used as *IM* for the mainshock fragility curves [27], aftershock fragility curves with Sa(T=0.3 s) in **Figure 11**(a) are not well fitted by the lognormal distribution with the standard deviation larger than 1 for the Red tag (DS_3) in **Table 3**. On the other hand, in **Figure 11**(b) and (c), PGV and Sa(T=0.5 s) show better performances of aftershock fragility curves for representing the cumulative damage effects than Sa(T=0.3 s). PGV and Sa(T=0.5 s) cover higher exceeding probabilities of post-DS_3 from pre-$DS_{0\text{-}1}$ than Sa(T=0.3 s) in **Figure 11**(b) and (c), respectively. All logarithmic standard deviations for different *IMs* in **Table 3** are increased from pre-DS_0 to pre-DS_2, and the standard deviations of aftershock fragility curves of Sa(T=0.3 s) and Sa(T=0.5 s) are higher than 0.8. This might suggest that stronger records of aftershocks are needed to include more points in the fragility curve development for Sa(T=0.3 s) and

Sa(T=0.5 s) in the range from 2 g to 3 g. Large standard deviations (e.g., 0.79) of state-dependent fragility curves were also observed from the back-to-back approach with IDA [50]. On the other hand, PGV shows a better performance for the development of aftershock fragility curves with standard deviations lower than 0.6. Overall, PGV is the most suitable *IM* for the cumulative damage aftershock fragility curves of the wood-frame houses.

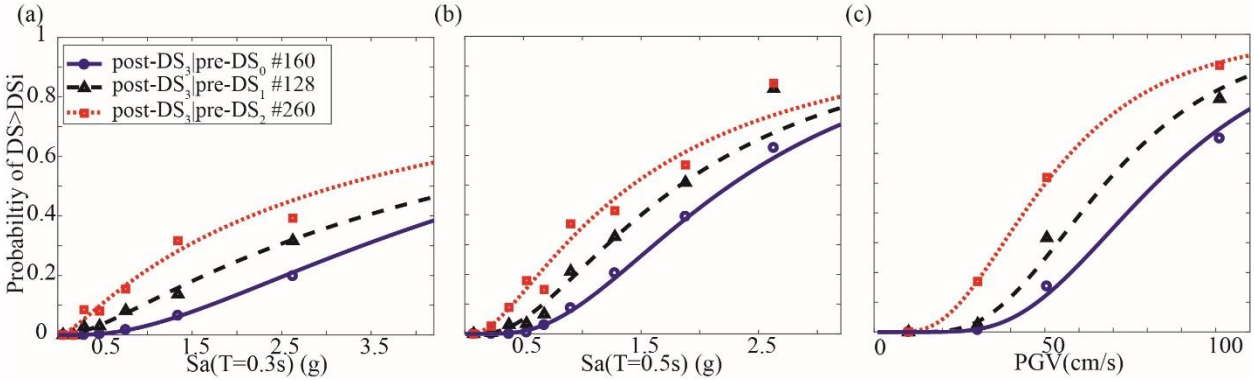

Figure 11. Plots of aftershock fragility curves for the post-DS_3 given pre-$DS_{0\text{-}2}$ with (a) Sa(T=0.3 s), (b) Sa(T=0.5 s), and (c) PGV based on pre-ResISDR and post-MaxISDR for House 4 and the lognormal distribution. The number of points exceeding post-DS_3 given pre-DS_0, pre-DS_1, and pre-DS_2 for House 4 is 160, 280, and 260, respectively.

Table 3. Median values (θ_{IM}) of mainshock-aftershock fragility curves for House 4 (standard deviations (β_{IM}) are shown in the parentheses) from the lognormal distribution.

	post-DS_1	post-DS_2	post-DS_3
House 4 (Sa(T=0.3 s))			
pre-DS_0 (MS)	0.51 (0.51)	1.24 (0.57)	1.83 (0.70)
pre-DS_0 (AS)	0.66 (0.62)	2.37 (0.80)	5.49 (0.92)
pre-DS_1 (AS)		1.26 (0.94)	4.71 (1.25)
pre-DS_2 (AS)			3.13 (1.47)
House 4 (Sa(T=0.5 s))			
pre-DS_0 (MS)	0.35 (0.30)	0.92 (0.32)	1.32 (0.46)
pre-DS_0 (AS)	0.33 (0.44)	1.04 (0.49)	2.26 (0.65)
pre-DS_1 (AS)		0.65 (0.65)	1.83 (0.79)
pre-DS_2 (AS)			1.43 (0.97)
House 4 (PGV)			
pre-DS_0 (MS)	17.84 (0.36)	44.73 (0.32)	63.35 (0.29)
pre-DS_0 (AS)	16.67 (0.47)	46.29 (0.45)	82.55 (0.43)
pre-DS_1 (AS)		28.93 (0.58)	67.80 (0.44)
pre-DS_2 (AS)			38.96 (0.60)

4.4 Comparison of aftershock fragility curves using the lognormal and multinomial distributions

In this subsection, the fragility curves using the multinomial distribution of House 4 of post-DS_3 given pre-DS_0 to pre-DS_2 with Sa(T=0.3 s), Sa(T=0.5 s), and PGV are shown in **Figure 12**(a), (b), and (c), respectively. All estimated parameters of the multinomial distribution are summarised in **Table 4**. Similar performances can be observed from the fixed *IM* bin counts of the lognormal distribution and multinomial distribution. Considering the inputs of the multinomial distribution fitting are *IMs* and post-DSs rather than the *IM* bins with certain exceeding probabilities from the lognormal distribution, the empirical distributions are counted such that the same number of data points of each bin is available. The number of data points in each bin is 5% of the total points given the same pre-DS but is constrained in the range of 50-200 in **Figure 12**. Although both fragility functions show good performances, the multinomial fitting is a better option. This is because the fixed *IM* bin counts from the lognormal distribution require a careful assessment of the histogram count of *IMs* given pre-DSs, and less than 10 *IM* bin counts are included to avoid the intersection of the same post-DS_i given pre-DSs. On the other hand, the multinomial distribution only requires *IM* and

post-DSs given each pre-DS_i to fit the curves progressively. Based on these considerations, the multinomial distribution is used to develop the aftershock fragility curves for the rest of the house models in the next subsection.

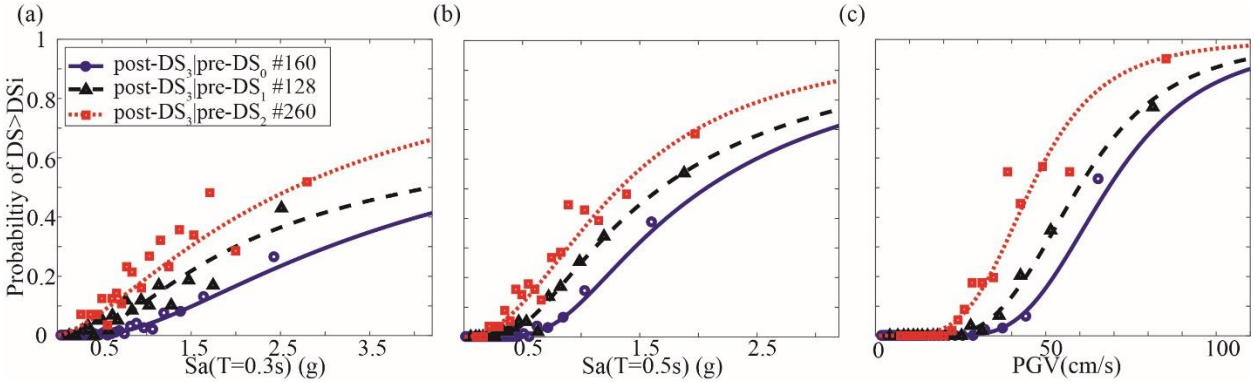

Figure 12. Plots of aftershock fragility curves for the post-DS_3 given pre-DS_{0-2} with (a) Sa(T=0.3 s), (b) Sa(T=0.5 s), and (c)PGV based on pre-ResISDR and post-MaxISDR for House 4 and the multinomial distribution. The number of points exceeding post-DS_3 given pre-DS_0, pre-DS_1, and pre-DS_2 for House 4 is 160, 280, and 260, respectively.

Table 4. Estimated parameters of mainshock-aftershock fragility curves of House 4 from the multinomial distribution.

	post-DS1	post-DS2	post-DS3
House 4 (Sa(T=0.3 s))			
pre-DS_0 (MS)	-2.48, -3.71	0.42, -2.75	-0.10, -1.34
pre-DS_0 (AS)	-1.42, -3.04	1.35, -1.87	1.25, -0.94
pre-DS_1 (AS)		0.31, -2.16	0.96, -0.76
pre-DS_2 (AS)			1.43, -1.46
House 4 (Sa(T=0.5 s))			
pre-DS_0 (MS)	-6.98, -6.75	-0.51, -5.66	0.15, -2.54
pre-DS_0 (AS)	-5.21, -4.70	-0.003, -3.58	1.18, -1.84
pre-DS_1 (AS)		-1.33, -2.93	0.77, -1.72
pre-DS_2 (AS)			0.59, -2.10
House 4 (PGV)			
pre-DS_0 (MS)	14.94, -5.18	21.76, -5.74	22.55, -5.54
pre-DS_0 (AS)	13.41, -4.82	18.15, -4.88	18.72, -4.47
pre-DS_1 (AS)		15.1806, -4.5396	17.63, -4.33
pre-DS_2 (AS)			16.91, -4.42

4.5 Aftershock fragility curves of Houses 1-3 with PGV

The plots of state-dependent fragility curves for Houses 1-3 are provided in **Figure 13**. By considering PGV as *IM* with the multinomial distribution, the fragility curves of Houses 1-4 (**Figure 12**(c) and **Figure 13**) show a good agreement with the description of seismic resistance in Section 2.3. For example, by looking at the PGV values with 50% exceeding probability of collapse state given intact conditions in **Figure 12**(c) and **Figure 13**, House 1 has the highest PGV value (110 cm/s), whereas the median value of PGV for House 4 is 65 cm/s. This indicates the better performance of the engineered OSB sheathing in comparison with horizontal board sheathing [34].

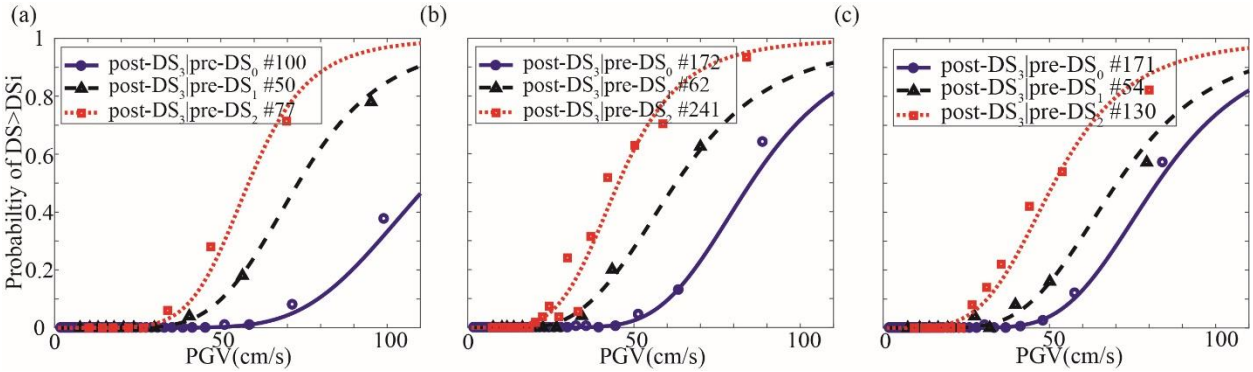

Figure 13. Plots of aftershock fragility curves for the post-DS_3 given pre-$DS_{0\text{-}2}$ with PGV based on pre-ResISDR and post-MaxISDR for (a) House 1, (b) House 2, and (c) House 3 with the multinomial distribution.

Table 5. Parameters θ_1 and θ_2 from the multinomial distribution for Houses 1-3.

	post-DS1	post-DS2	post-DS3
House 1 (PGV)			
pre-DS_0 (MS)	15.49, -4.29	25.40, -5.78	28.85, -6.17
pre-DS_0 (AS)	14.25, -4.28	17.70, -4.07	24.64, -5.30
pre-DS_1 (AS)		16.99, -4.80	23.57, -5.50
pre-DS_2 (AS)			26.06, -6.41
House 2 (PGV)			
pre-DS_0 (MS)	16.92, -5.16	24.23, -5.94	27.95, -6.33
pre-DS_0 (AS)	15.74, -5.10	19.94, -5.00	24.44, -5.54
pre-DS_1 (AS)		19.92, -6.18	17.46, -4.22
pre-DS_2 (AS)			18.30, -4.80
House 3 (PGV)			
pre-DS_0 (MS)	16.33, -5.15	23.48, -5.78	26.17, -5.98
pre-DS_0 (AS)	15.21, -5.08	19.14, -4.82	22.00, -5.04
pre-DS_1 (AS)		14.33, -4.04	19.19, -4.54
pre-DS_2 (AS)			17.44, -4.43

4.6 Application for state-dependent fragility curves to the Cascadia subduction zone

To demonstrate an application of the state-dependent fragility curves, an example of a M_w 9.0 mainshock followed by a M_w 6.0 crustal aftershock [51] in the CSZ is considered. PGVs for the M_w 9.0 mainshock scenario (rupture distance of 70 km) and the M_w 6.0 crustal aftershock scenario (Joyner and Boore distance of 8 km) are calculated for the City of Victoria, Canada with V_{s30}=450 m/s using GMPEs [42,52].

Using the simulation-based seismic hazard and risk approach [53], the PGV from a M_w 9.0 event can be applied to the MS fragility curves to estimate the post-$DS_{i,1}$ (post-DS_i after the 1st event which is the same notation as in **Figure 1**). The post-$DS_{i,1}$ due to the first event is equivalent as pre-$DS_{i,2}$ (pre-DS_i before the second event). Following that, pre-$DS_{i,2}$ and the PGV of the aftershock would be the input information to select the state-dependent fragility curves of aftershocks to estimate the post-$DS_{i,2}$. Subsequently, more aftershocks can be considered to estimate the DS of the house model after each subsequent aftershock. The state-dependent fragility curves allow to estimate the DS of the house model after each event sustaining the same DS or reaching a higher level of DS given *IM*.

In total 10,000 simulations are carried out. Each simulation has PGVs of the M_w 9.0 mainshock followed by the M_w 6.0 crustal aftershock. Following that, the PGV of mainshock and aftershocks are randomly sampled from the fragility curves to calculate the DS after the mainshocks and aftershocks. The damage probabilities of Houses 1-4 by the M_w 9.0 mainshock and the MSAS sequences based on 10,000 simulations are shown in **Figure 14**a and b, respectively. By including the crustal aftershocks, the probabilities that Houses 1-4 are changed from DS_0 (no damage) to DS_1 (Green tag) are 18.1%, 18.6%, 18.6%, and 14.0%. Compared with the damage probability of the mainshock, additional 6.4%, 12.3%, 9.3%, and 12.3% of Houses 1-4 could change to DS_2 (Yellow tag) by the crustal aftershock,

whereas the probabilities that the crustal aftershock causes additional damage of DS_3 (Red tag) are 1.1%, 3.3%, 2.5%, and 4.8% in comparison with the mainshock for Houses 1-4.

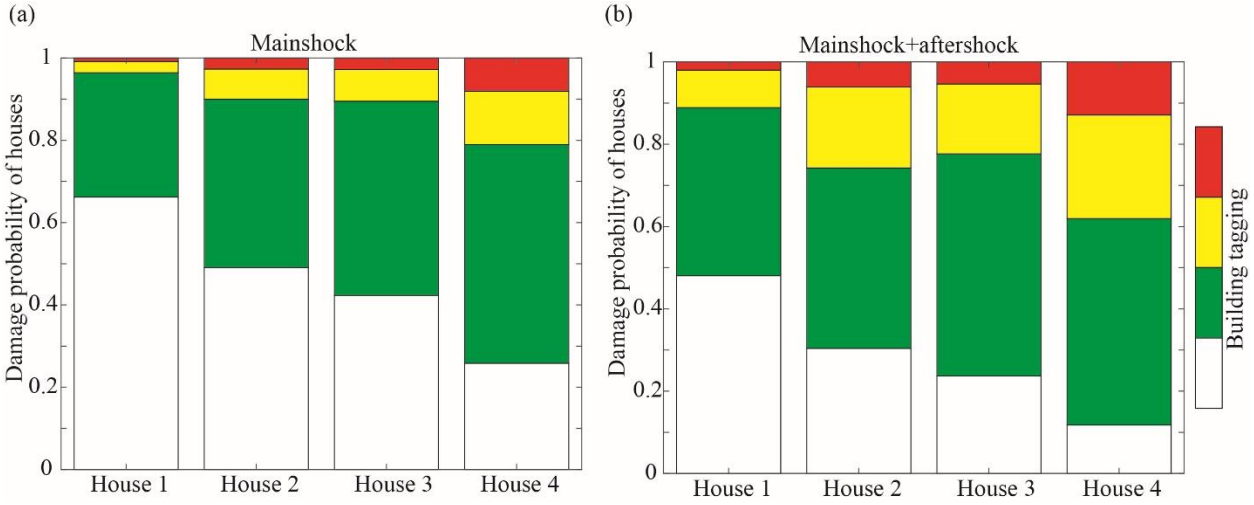

Figure 14. Damage probability of Houses 1-4 by (a) M_w 9.0 mainshock with 70km rupture distance and (b) M_w 9.0 mainshock and M_w 6.0 crustal aftershock with Joyner-Boore distance=8 km and V_{s30}=450 m/s.

5 CONCLUSIONS

This study developed a new approach to produce the state-dependent fragility curves. To capture the real characteristics of aftershocks in the cumulative damage assessments of mainshock and aftershock sequences, the *pre-EDP* combining with *IM* and *post-EDP* as a 3D dataset was introduced for developing the state-dependent aftershock fragility curves. The UBC-SAWS model was used to demonstrate the new approach for the state-dependent fragility curves of the wood-frame houses using 596 real MSAS records with cloud analysis. The selection of *IMs* (Sa, AI, CAV, PGV, and SI) and *EDPs* (ResISDR, MaxISDR, and MaxIISDR) for wood-frame houses was discussed in this study. To account for the cumulative damage after $event_n$, the pre-ResISDR and post-MaxISDR are considered to be the most suitable *EDPs* to represent the *pre-EDP* and *post-EDP*, respectively. To evaluate different *IMs*, the efficiency, sufficiency, and relative sufficiency were evaluated for each *IM*. Sa(T=0.3-0.5 s) and PGV show better performances than other *IMs*.

The MSAS fragility curves were developed with pre-ResISDR and post-MaxISDR by considering *IMs* (Sa(T=0.3 s), Sa(T=0.5 s), and PGV). PGV showed a better performance to capture the cumulative damage effects of aftershocks for the wood-frame structure using real MSAS sequences than other *IMs*. Different fragility functions (the lognormal and multinomial distributions) were also compared. The multinomial distribution was considered as more suitable to fit the fragility curves than the lognormal distribution, because the former does not require careful bin counts to avoid the intersections of aftershock fragility curves for post-DS conditioned on different pre-DSs. Combining the building-tagging-based DS definitions with the multinomial distribution lead to the development of robust aftershock fragility curves.

The limitations of the aftershock fragility curves include that (1) more destructive aftershock records should be included to have a better fitting of fragility models with a smaller logarithmic standard deviation for Sa(T=0.3 s) and Sa(T=0.5 s), (2) when more destructive aftershock records are included, ground motion records could be further classified by earthquake types, so aftershock fragility curves can be developed by crustal and subduction-zone records which represent the different spectra shapes between the crustal and subduction-zone earthquakes, and (3) the SAWS model does not incorporate in-cycle degradation. A further investigation of the impact of in-cycle degradation on the development of fragility curves is necessary in the future study.

The developed aftershock fragility curves of Houses 1-4 can be employed to estimate the DSs implementing a spatiotemporal risk assessment for a M_w 9.0 mainshock triggering both crustal and subduction-zone aftershocks (e.g., [54]) in British Colombia, Canada. The evaluated PGV and real MSAS sequences facilitate the estimation of cumulative damage of wood-frame houses. The outputs of the risk assessment provide not only the likelihood of the DSs on the day of the inspection for building tagging [55] but also daily forecasts of the DSs in a short-time period after the inspection day. This can be part of inspection combing with the conventional building tagging (e.g., residual

displacement check of the structure components) and providing additional information for the structural inspector. In addition, a future direction of the development of state-dependent fragility curves could be to develop an approach to construct 'realistic MS-AS sequences' either using real records with careful record selection or simulating records as mainshock-aftershock sequence for the Cascadia subduction zone (e.g., [24]).

ACKNOWLEDGEMENTS

The authors gratefully acknowledge financial support from the Leverhulme Trust (RPG-2017-006) for the Global Earthquake Resilience for Natural-Engineering-Social Interacting Systems (GENESIS) project. The second author is supported by the Canada Research Chair in Multi-Hazard Risk Assessment program at Western University (950-232015) and the NSERC Discovery Grant (RGPIN-2019-05898). Ground motion data for Japanese earthquakes and worldwide crustal earthquakes were obtained from the K-NET/KiK-net/ SK-net databases at http://www.kyoshin.bosai.go.jp/ and http://www.sknet.eri.u-tokyo.ac.jp/, and the PEER-NGA database at http://peer.berkeley.edu/nga/index.html, respectively.

REFERENCES

1. Goda K, Pomonis A, Chian SC, Offord M, Saito K, Sammonds P, *et al.* Ground motion characteristics and shaking damage of the 11th March 2011 M w 9.0 Great East Japan earthquake. *Bulletin of Earthquake Engineering* 2013; **11**(1): 141–170.
2. Kazama M, Noda T. Damage statistics (Summary of the 2011 off the Pacific Coast of Tohoku Earthquake damage). *Soils and Foundations* 2012; **52**(5): 780–792.
3. Yeo GL, Cornell CA. Building tagging criteria based on aftershock PSHA. *13th World Conference on Earthquake Engineering*, 2004.
4. Bazzurro P, Cornell CA, Menun C, Motahari M. Guidelines for seismic assessment of damaged buildings. *13th World Conference on Earthquake Engineering*, 2004.
5. Yeo GL, Cornell CA. Post-quake decision analysis using dynamic programming. *Earthquake Engineering & Structural Dynamics* 2009; **38**(1): 79–93.
6. Iervolino I, Giorgio M, Chioccarelli E. Closed-form aftershock reliability of damage-cumulating elastic-perfectly-plastic systems. *Earthquake Engineering & Structural Dynamics* 2014; **43**(4): 613–625.
7. Ebrahimian H, Jalayer F, Asprone D, Lombardi AM, Marzocchi W, Prota A, *et al.* A performance-based framework for adaptive seismic aftershock risk assessment. *Earthquake Engineering & Structural Dynamics* 2014; **43**(14): 2179–2197.
8. Goldfinger C, Nelson CH, Morey a. E, Joel E J, Patton J, Karabanov E, *et al.* Turbidite event history — methods and implications for holocene paleoseismicity of the Cascadia Subduction Zone. *US Geological Survey Professional Paper 1661-F* 2012: 170 p.
9. Verderame GM, Ricci P, De Luca F, Del Gaudio C, De Risi MT. Damage scenarios for RC buildings during the 2012 Emilia (Italy) earthquake. *Soil Dynamics and Earthquake Engineering* 2014; **66**: 385–400.
10. Luco N, Bazzurro P, Cornell CA. Dynamic versus static computation of the residual capacity of a mainshock-damaged building to withstand an aftershock. *13th World Conference on Earthquake Engineering* 2004.
11. Jalayer F, Ebrahimian H. Seismic risk assessment considering cumulative damage due to aftershocks. *Earthquake Engineering & Structural Dynamics* 2017; **46**(3): 369–389.
12. Raghunandan M, Liel AB, Luco N. Aftershock collapse vulnerability assessment of reinforced concrete frame structures. *Earthquake Engineering & Structural Dynamics* 2015; **44**(3): 419–439.
13. Goda K. Record selection for aftershock incremental dynamic analysis. *Earthquake Engineering & Structural Dynamics* 2015; **44**(7): 1157–1162.
14. Cornell CA, Asce M, Jalayer F, Hamburger RO, Foutch D a. Probabilistic basis for 2000 SAC Federal Emergency Management Agency steel moment frame guidelines 2002; **128**(4): 526–533.
15. Luco N, Cornell CA. Structure-specific scalar intensity measures for near-source and ordinary earthquake ground motions. *Earthquake Spectra* 2007; **23**(2): 357–392.
16. Luco N. Probabilistic seismic demand analysis, SMRF connection fractures, and near-source effects, *Ph.D. thesis*, Department of Civil and Environmental Engineering, Stanford University, 2002.
17. Bradley BA. Empirical equations for the prediction of displacement spectrum intensity and its correlation with other intensity measures. *Soil Dynamics and Earthquake Engineering* 2011; **31**(8): 1182–1191.
18. Vamvatsikos D, Cornell CA. Incremental dynamic analysis. *Earthquake Engineering & Structural*

Dynamics 2002; **31**(3): 491–514.
19. Goda K, Salami MR. Inelastic seismic demand estimation of wood-frame houses subjected to mainshock-aftershock sequences. *Bulletin of Earthquake Engineering* 2014; **12**(2): 855–874.
20. Baker JW. Efficient analytical fragility function fitting using dynamic structural analysis. *Earthquake Spectra* 2015; **31**(1): 579–599.
21. De Risi R, Goda K, Yasuda T, Mori N. Is flow velocity important in tsunami empirical fragility modeling? *Earth-Science Reviews* 2017; **166**: 64–82.
22. Ventura CE, Finn WDL, Onur T, Blanquera A, Rezai M. Regional seismic risk in British Columbia : classification of buildings and development of damage probability functions. *Canadian Journal of Civil Engineering* 2005; **32**(2): 372–387.
23. Iervolino I, Giorgio M, Chioccarelli E. Markovian modeling of seismic damage accumulation. *Earthquake Engineering & Structural Dynamics* 2016; **45**(3): 441–461.
24. Goda K, Taylor CA. Effects of aftershocks on peak ductility demand due to strong ground motion records from shallow crustal earthquakes. *Earthquake Engineering & Structural Dynamics* 2012; **41**(15): 2311–2330.
25. Goda K, Wenzel F, De Risi R. Empirical assessment of non-linear seismic demand of mainshock-aftershock ground-motion sequences for Japanese earthquakes. *Frontiers in Built Environment* 2015; **1**: 6. DOI: 10.3389/fbuil.2015.00006.
26. Halchuk S, Allen TI, Adams J, Rogers GC. Fifth generation seismic hazard model input files as proposed to produce values for the 2015 National Building Code of Canada. *Geological Survey of Canada, Open File* 2014.
27. Goda K, Atkinson GM. Seismic performance of wood-frame houses in south-western British Columbia. *Earthquake Engineering & Structural Dynamics* 2011; **40**(8): 903–924.
28. Jalayer F, De Risi R, Manfredi G. Bayesian Cloud Analysis: efficient structural fragility assessment using linear regression. *Bulletin of Earthquake Engineering* 2015; **13**(4): 1183–1203.
29. Lagaros ND, Fragiadakis M. Fragility assessment of steel frames using neural networks. *Earthquake Spectra* 2007; **23**(4): 735–752.
30. White TW, Ventura CE. Seismic performance of wood-frame residential construction in British Columbia-technical report. *Earthquake Eng. Research Facility Report No. 06-03,* University of British Columbia, Vancouver, Canada, 2006.
31. Folz B, Filiatrault A. Seismic analysis of woodframe structures. I: Model formulation. *Journal of Structural Engineering* 2004; **130**(9): 1353–1360.
32. Folz B, Filiatrault A. Seismic analysis of woodframe structures. II: Model implementation and verification. *Journal of Structural Engineering* 2004; **130**(9): 1361–1370.
33. Folz B, Filiatrault A. Cyclic analysis of wood shear walls. *Journal of Structural Engineering* 2001; **127**(4): 433–441.
34. Pan Y, Ventura CE, Finn WDL. Effects of ground motion duration on the seismic performance and collapse rate of light-frame wood houses. *Journal of Structural Engineering* 2018; **144**(8), 04018112-1.
35. Ebrahimian H, Jalayer F, Lucchini A, Mollaioli F, Manfredi G. Preliminary ranking of alternative scalar and vector intensity measures of ground shaking. *Bulletin of Earthquake Engineering* 2015; **13**(10): 2805–2840.
36. Porter K, Scawthorn CR, Beck JL. Cost-effectiveness of stronger woodframe buildings. *Earthquake Spectra* 2006; **22**(1): 239–266.
37. Charvet I, Ioannou I, Rossetto T, Suppasri A, Imamura F. Empirical fragility assessment of buildings affected by the 2011 Great East Japan tsunami using improved statistical models. *Natural Hazards* 2014; **73**(2): 951–973.
38. Jalayer F, Beck JL, Zareian F. Analyzing the sufficiency of alternative scalar and vector intensity measures of ground shaking based on information theory. *Journal of Engineering Mechanics* 2012; **138**(3): 307–316.
39. Christovasilis IP, Filiatrault A, Constantinou MC, Wanitkorkul A. Incremental dynamic analysis of woodframe buildings. *Earthquake Engineering & Structural Dynamics* 2009; **38**(4): 477–496.
40. Mollaioli F, Lucchini A, Cheng Y, Monti G. Intensity measures for the seismic response prediction of base-isolated buildings. *Bulletin of Earthquake Engineering* 2013; **11**(5): 1841–1866.
41. Abrahamson N, Gregor N, Addo K. BC Hydro ground motion prediction equations for subduction earthquakes. *Earthquake Spectra* 2016; **32**(1): 23–44.
42. Ghofrani H, Atkinson GM. Ground-motion prediction equations for interface earthquakes of M7 to M9 based on empirical data from Japan. *Bulletin of Earthquake Engineering* 2014; **12**(2): 549–571.
43. Christidis AA, Dimitroudi EG, Hatzigeorgiou GD, Beskos DE. Maximum seismic displacements evaluation

of steel frames from their post-earthquake residual deformation. *Bulletin of Earthquake Engineering* 2013; **11**(6): 2233–2248.
44. Tesfamariam S, Goda K. Seismic performance evaluation framework considering maximum and residual inter-story drift ratios: application to non-code conforming reinforced concrete buildings in Victoria, BC, Canada. *Frontiers in Built Environment* 2015; **1**(18). DOI: 10.3389/fbuil.2015.00018.
45. Federal Emergency Management Agency (FEMA). Prestandard and commentary for the seismic rehabilitation of buildings. *Report No. FEMA-356*, Washington, DC, 2000.
46. Nazari N, Van De Lindt JW, Li Y. Effect of mainshock-aftershock sequences on woodframe building damage fragilities. *Journal of Performance of Constructed Facilities* 2013; **29**(1), 04014036-1.
47. Federal Emergency Management Agency (FEMA). Seismic performance assessment of buildings. *Report No. FEMA P-58*, Washington, DC, 2014.
48. Rudolf J, Ventura CE, Prion H. Static and dynamic testing of shear wall panels for typical wood frame residential construction in British Columbia, 1998.
49. Lallemant D, Kiremidjian A, Burton H. Statistical procedures for developing earthquake damage fragility curves. *Earthquake Engineering & Structural Dynamics* 2015; **44**(9): 1373–1389.
50. Raghunandan M. Influence of long duration ground shaking on collapse of reinforced concrete structures, *Ph.D. thesis*, Department of Civil, Environmental, and Architectural Engineering, University of Colorado, 2013.
51. Morell KD, Regalla C, Leonard LJ, Amos C, Levson V. Quaternary rupture of a crustal fault beneath Victoria, British Columbia, Canada. *GSA Today* 2017; **27**. DOI: 10.1130/GSATG291A.1.
52. Boore DM, Stewart JP, Seyhan E, Atkinson GM. NGA-West2 equations for predicting PGA, PGV, and 5% damped PSA for shallow crustal earthquakes. *Earthquake Spectra* 2014; **30**(3): 1057–1085.
53. Goda K. Assessment of Seismic Hazard and Risk, and Decision-Making under Uncertainty, *Ph.D. thesis*, Department of Civil and Environmental Engineering, University of Western Ontario, 2007.
54. Zhang L, Werner MJ, Goda K. Spatiotemporal seismic hazard and risk assessment of aftershocks of M 9 megathrust earthquakes. *Bulletin of the Seismological Society of America* 2018; **108**(6): 3313–3335.
55. Luco N, Gerstenberger MC, Uma SR, Ryu H, Liel AB, Raghunandan M. A methodology for post-mainshock probabilistic assessment of building collapse risk. *Ninth Pacific Conference on Earthquake Engineering, Auckland, New Zealand*, 2011.